Polymer 300 (2024) 126986

Contents lists available at ScienceDirect

Polymer

journal homepage: www.elsevier.com/locate/polymer

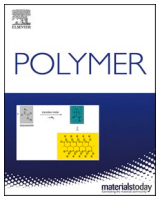

Transport properties of ethylene glycol functionalized membranes exposed to nonaqueous electrolytes

Charles R. Leroux [a], Patrick M. McCormack [a,1], Shruti Elango [a,b], Geoffrey M. Geise [a,*], Gary M. Koenig Jr. [a,**]

[a] Department of Chemical Engineering, University of Virginia, 385 McCormack Rd., Charlottesville, Virginia, 22903, United States
[b] Department of Chemistry, University of Virginia, 409 McCormack Rd., Charlottesville, VA, 22903, United States

ARTICLE INFO

Keywords:
Redox flow battery
Lithium
Selective separator

ABSTRACT

Non-aqueous redox flow batteries (RFBs) are a promising technology to meet growing demand for grid-scale energy storage. Membrane separators, designed specifically for use with organic solvents, are necessary to advance non-aqueous RFBs. Herein, we report the development of a series of poly(phenylene oxide) (PPO) membranes functionalized with poly(ethylene glycol) (PEG) side chains to investigate the influence of PEG side chain length and degree of PEGylation on membrane transport properties. Increasing the degree of PEGylation generally led to increases in electrolyte uptake, hydroxy TEMPO permeability, and ionic conductivity likely caused by an increase in overall PEG content, as opposed to specific interactions caused by changing the degree of PEGylation. For membranes with similar PEG content, increasing the length of the PEG side chain resulted in decreases in electrolyte uptake, permeability, and conductivity possibly due to differences in the solvation behavior of the PEG chains with different lengths.

1. Introduction

Growing concern over the rising impact of global climate change has led to significant advances in renewable energy technologies. Solar cells have achieved increased efficiency and decreased cost enabling significant growth in implementation worldwide [1,2]. Increased use of solar power and other renewable energy sources creates challenges for grid power management due to the inherent intermittency of these technologies [2–8]. Economically viable grid scale energy storage technologies are necessary to enable the continued deployment of clean energy technologies into the power grid, and redox flow battery (RFB) technology has received significant attention to address this need [7,9–13].

RFBs store energy electrochemically, but RFBs are unique batteries in that they typically rely on redox active materials dissolved in a liquid electrolyte instead of solid electroactive materials (Fig. 1) [8,10,14]. In RFBs, the electrolytes containing the dissolved redox active materials (anolyte and catholyte) are pumped from storage tanks through the power stack where the active materials undergo oxidation and reduction reactions at the electrode-electrolyte interface to charge/discharge the battery [6,8]. These redox reactions generally are isolated within the electrodes of the power stack, and thus the two major metrics of the battery, the power (stack/active area) and the energy (capacity/volume of storage tanks), are considered decoupled [3,5,10,15]. Decoupling these components results in a major advantage for RFBs; the capacity and power of the battery can be tuned independently and in principle in a modular fashion [3,5,10,15].

The energy density of RFBs, especially more mature aqueous RFB technologies, is limited by low cell voltage and low solubility of redox active materials [16]. Towards increasing the cell voltage, researchers are investigating RFBs that utilize non-aqueous electrolytes to overcome the inherent thermodynamic electrochemical stability limit of water (~1.23 V) [3,8,16,17]. Therefore, non-aqueous electrolytes, which can have wider potential ranges of thermodynamic stability, allow nonaqueous RFBs to operate at higher voltages compared to aqueous electrolyte RFBs. In addition to higher operating voltages afforded by non-aqueous versus aqueous electrolytes, the redox active materials

* Corresponding author.
** Corresponding author.
E-mail addresses: kvm8bz@virginia.edu (C.R. Leroux), pmccormack32@gmail.com (P.M. McCormack), se2ezr@virginia.edu (S. Elango), geise@virginia.edu (G.M. Geise), gary.koenig@virginia.edu (G.M. Koenig).
[1] Current Affiliation: Feon Energy, Inc., 150 New Boston St STE W, Woburn, MA 01801, United States.

https://doi.org/10.1016/j.polymer.2024.126986
Received 27 January 2024; Received in revised form 22 March 2024; Accepted 26 March 2024
Available online 29 March 2024

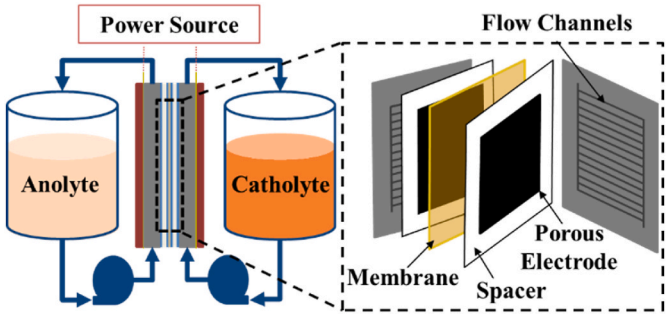

Fig. 1. Schematic of a typical redox flow battery where (left) electrolyte solutions containing dissolved redox active materials are circulated between storage tanks and power stack. Inside the (right) power stack, the components include electrodes, membrane separators, and flow fields.

need to be present in the electrolyte at sufficiently high concentrations. Thus, in some cases, redox active material solubility is a limiting factor. New chemistry for redox active materials, use of deep eutectic solvents, or using liquid redox active materials are all approaches under consideration with nonaqueous RFBs for addressing redox active material solubility challenges [11,18–20]. These approaches have enabled redox active material concentrations that exceed 4 M in organic electrolytes [6,21]. However, in many cases, these gains in redox active material solubility, which are favorable for RFB operation, come at the expense of higher solution viscosity and resistance, which can be detrimental to overall operation of the RFB [13].

In addition to the choices of solvent and redox active material, the economics and battery performance of non-aqueous RFBs are limited by membrane separator properties [17]. The development of an RFB with long cycle life and high energy, voltage, and coulombic efficiency requires a membrane separator that offers long-term chemical stability in non-aqueous electrolyte, high ionic conductivity (~1.3 mS/cm for a 30 μm thick membrane), and low redox active material permeability ($\sim 10^{-10}$ cm^2/s) [10,17,22]. Many RFB separators are based on ion exchange membranes (IEMs). IEMs rely on fixed charged groups along a polymer backbone to provide charge carriers that facilitate ion transport [23,24]. Conductivity generally can be increased by increasing the density of fixed charges in the membrane so long as the concentration of ions that dissociate from the fixed charges (i.e., the concentration of charge carriers in the polymer) increases as a result of this modification [3,17,25]. Another mechanism commonly employed to increase the conductivity of IEMs is the incorporation of flexible polymeric spacers between the polymer backbone and the fixed charge group of the membrane [17,25]. Incorporating flexible side chains may lead to nanoscale phase separation such that clusters of fixed charge groups form ion conducting pathways through the polymer matrix [17,25–29].

IEMs have yet to meet targeted nonaqueous RFB conductivity and permeability properties. Pursuits towards incorporating different membrane functional groups could lead to improved membrane properties. Here, we report a polymer membrane where ionic conductivity is provided by flexible, polar poly(ethylene glycol) (PEG) side chains as opposed to fixed charges. High molecular weight PEG chains (>10,000 g/mol) are commonly used in solid polymer electrolytes (SPEs) due to PEG characteristics including a low glass transition temperature (~−65 °C), favorable interactions with Li^+, low toxicity, and stability while in contact with lithium metal [26,30–36]. Interactions between Li^+ and the ethylene glycol (EG) repeat units of PEG are well documented in dry polymers and polymer gels [26,30,31,36,37]. The ether groups of the side chains interact favorably with Li^+ via coordination involving 4 to 6 PEG repeat units per Li^+, and ion transport between coordination sites leads to conductivity [36].

Similar to IEMs, conductivity increases with increasing PEG content in the polymer and with increasing temperature [30,36]. Increased conductivity can result from enhanced connectivity of conductive regions of the polymer (as PEG content increases) and polymer chain segmental dynamics are facilitated as temperature increases, which further promotes Li^+ conduction [36]. Chain mobility and its effect on ionic conduction can be enhanced further by solvating the polymer, as would be typical in use in an RFB. A potential limitation of using SPE polymers in RFB applications is low dimensional stability that may occur upon solvation by many common non-aqueous electrolyte solvents [36].

Here, membranes were prepared by functionalizing a poly(phenylene oxide) (PPO) backbone with flexible poly(ethylene glycol) (PEG) side chains. The PPO backbone provides dimensional stability when the material is exposed to organic solvents and may facilitate low redox active material permeability [3,38,39]. The flexible PEG side chains, on the other hand, promote conductivity [3]. The side chain length and overall PEG content of the membrane was systematically varied using three different molecular weights of PEG oligomers and three different degrees of PPO PEGylation. This series of materials facilitated study of the influence of both the degree of PEGylation and the PEG side chain length on the electrolyte uptake, redox active material permeability, and ionic conductivity of the polymer exposed to a nonaqueous electrolyte.

2. Materials and methods

2.1. Br-PPO synthesis

Poly(2,6-dimethyl-1,4-phenylene oxide) (PPO, SKU 181781, Sigma-Aldrich) was brominated via a free radical reaction utilizing *N*-bromosuccinimide (NBS, 99% Sigma Aldrich) as the bromine source and azobisisobutyronitrile (AIBN, 98% Sigma-Aldrich) as the initiator [39]. Three different degrees of bromination were synthesized (x = 9, 14, and 18, Scheme 1). For each reaction the amount of NBS used was scaled to obtain the target degrees of bromination based on prior experiments (the scaling relationship is provided in the Supporting Information, Fig. S1). In each case, 6 g of PPO and 0.056 g of AIBN per gram of NBS were used. The PPO was first dissolved in 75 mL of chlorobenzene at room temperature then placed in an oil bath at 110 °C. The NBS and AIBN were pre-weighed and evenly distributed into 4 separate glass vials. Each vial of mixed NBS and AIBN powder was added to the reaction flask containing the PPO solution at 15-min intervals over the course of 45 min. After all the NBS and AIBN powder was added to the reaction flask, the reaction proceeded at 110 °C for 30 min (total reaction time of 75 min).

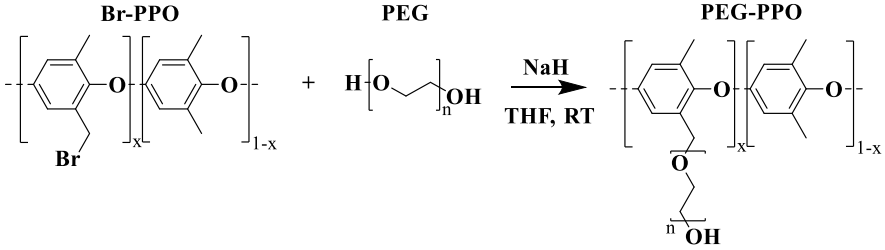

Scheme 1. Williamson Ether synthesis in tetrahydrofuran using sodium hydride (NaH) at room temperature (RT) to combine Br-PPO and PEG to form PEG-PPO.

The product was collected by precipitating the reaction mixture in 10-fold excess reagent alcohol (Fisher Chemical). The polymer was collected by filtration and dried under vacuum to remove the alcohol. For further purification the polymer was dissolved in 50 mL of chloroform. Precipitation in reagent alcohol was repeated and the polymer was filtered and dried under vacuum at room temperature for 24 h.

2.1.1. PEGylation of Br-PPO

The brominated PPO (Br-PPO) was functionalized with hydroxyl group terminated poly(ethylene glycol) (PEG, Sigma-Aldrich) via Williamson-Ether synthesis to form PEG-PPO with a remaining free hydroxyl group at the end of the PEG chain (Scheme 1) [40]. The PEG chain length was varied using 3 different molecular weight PEG chains of 200, 400, and 600 g/mol (the corresponding average chain lengths, n in Scheme 1, were 4.5, 9, and 13.6, respectively). The Williamson-Ether Synthesis was performed with 1.5 g of Br-PPO, 15x molar excess PEG (Sigma Aldrich), and 1.5x molar excess sodium hydride (NaH, Sigma Aldrich, 60% dispersion in mineral oil) per equivalent of bromine in the intermediate Br-PPO. It was critical to prevent water contamination, as NaH can be consumed by residual water resulting in a lower extent of reaction. Therefore, all materials were dried for 24–48 h prior to the start of the reaction. PEG was mixed with tetrahydrofuran (THF, ≥99% (250 ppm BHT) Sigma-Aldrich) at concentrations ranging from 0.2 to 0.25 mg (PEG)/mL (THF) (exact quantities and resulting experimental degrees of PEGylation can be found in the Supporting Information, Table S1). The PEG concentration was maintained within this range to ensure solubility of the products and reactants in THF was maintained throughout the synthesis. The solution of PEG dissolved in THF as well as any additional THF used in the reaction was dried via contact of the solution with molecular sieves (3 Å, Alfa Aesar) for 48 h. Additionally, the 1.5 g of Br-PPO and all glassware required for the reaction was dried under vacuum at 80 °C for 24 h.

To perform the reaction, NaH was weighed and placed in a 3-neck flask. The flask was placed in an ice bath and purged with nitrogen. Using a pressure equalizing addition funnel, 5–10 mL of dry THF was added to disperse the NaH. Then, the PEG solution was added over a period of approximately 30 s while maintaining flow of nitrogen through the flask. The reaction proceeded for 30 min under a nitrogen atmosphere. Br-PPO was dissolved in 50 mL of THF and slowly added to the reaction flask using a pressure equalizing addition funnel while maintaining flow of nitrogen. After all the dissolved Br-PPO was added, the flask was removed from the ice bath and allowed to react at room temperature for 24 h under a nitrogen atmosphere. After 24 h, the solution was precipitated in 10-fold excess isopropyl alcohol (IPA, 99.5% VWR) by volume and collected via filtration. To improve product purity, the filtrate was rinsed with IPA (using half of the volume used for precipitation) in a Buchner funnel. The product was dispersed in 25 mL of reagent alcohol and dried in an evaporating dish in a fume hood for 2 h before being dried under vacuum at room temperature for approximately 16 h.

2.2. Polymer characterization

2.2.1. Structural analysis

Structural characterization of Br-PPO and PEG-PPO polymer materials was performed using proton nuclear magnetic resonance (^{1}H NMR, Varian 600 MHz) spectroscopy (Fig. S2). For all materials, $CDCl_3$ (99.8% deuterated, Sigma-Aldrich) was used as the solvent. Spectra were collected from 10 mg of sample that was dissolved in 1 mL of the deuterated solvent.

2.2.2. Thermal analysis

Differential scanning calorimetry (DSC) was used to determine glass transition temperature (T_g) values for the membranes. A mass of 5–10 mg of dry membrane was characterized by scanning twice from −100 °C to 200 °C at a scan rate of 10 °C per minute. The first scan was performed to clear the thermal history of the glassy polymer and to remove any excess solvent present in the sample. The T_g values were obtained during the second scan using the midpoint between inflection points on the thermogram (Fig. S3) indicating a transition within the polymer. Glass transition temperatures were used to estimate PEG content, w_{PEG}, by comparing the measured PEG-PPO T_g value to the homopolymer glass transition temperatures of PEG, $T_{g,PEG}$, and PPO, $T_{g,PPO}$, using the Fox Equation [41]:

$$\frac{1}{T_g} = \frac{w_{PEG}}{T_{g,PEG}} + \frac{(1 - w_{PEG})}{T_{g,PPO}} \quad 2)$$

2.3. Membrane casting procedure

Membranes were cast from solution. First, 0.15 g of dry PEG-PPO was dissolved in 6 mL of chloroform. Then, this solution was poured into a 6 cm diameter polytetrafluoroethylene (PTFE) dish (Fisher Scientific). The dish was placed in a 40 °C convection oven for 1 h to allow most of the solvent to evaporate, forming the membrane. Next, the membrane was removed from the PTFE dish, placed loosely back in the dish, and dried under vacuum at room temperature for a minimum of 16 h to remove residual solvent. Membranes were cast to a nominal thickness of 40–60 μm.

2.4. Ion transport

To characterize the materials as selective and conductive membranes when immersed in organic electrolytes, lithium bis(fluorosulfonyl)imide (LiFSI, Nippon Shokubai) was selected as the electrolyte salt and acetonitrile (ACN, 99.9% Fisher) was selected as the solvent. This electrolyte offers relatively high conductivity and low viscosity (1.6 M LiFSI in ACN has a conductivity of around 70 mS/cm at 60 °C and a viscosity of ~0.7 cP at 60 °C), which makes the electrolyte potentially attractive for energy storage applications [42].

Ionic conductivity of the membranes was determined using electrochemical impedance spectroscopy (EIS). The membranes were first dried under vacuum at room temperature for approximately 16 h, then soaked for 24 h in electrolyte solution (ranging from 0.5–2 M LiFSI in ACN). EIS measurements were conducted using electroless nickel immersion gold coated copper electrodes, with a diameter of 1.27 cm. Temperature would likely impact both the membrane conductivity and permeability and thus selectivity properties [43,44], but in this study, EIS was performed at room temperature (22 °C) to be consistent with other studies of IEMs for RFBs [17,24,25,45]. EIS was assessed in a through-plane geometry over a frequency range between 7 MHz and 100 Hz with an amplitude of 10 mV using a Biologic Instrument SP300 potentiostat. The measurements were conducted with the membrane confined within a controlled environment sample holder.

Cell resistance was determined using the high frequency intercept of the EIS Nyquist plot (representative data are reported in the Supporting Information as Fig. S4) [46–48]. The blank cell resistance (i.e., the cell without a membrane separator) was subtracted from each cell resistance value measured with a membrane to determine the membrane resistance (R). The conductivity was then calculated by using the membrane resistance and membrane thickness (L) and active area (A) as:

$$\text{Conductivity} = \frac{L}{A * R} \quad 3)$$

2.5. Redox active material permeability

A representative redox active material, 4-hydroxy-2,2,6,6-tetramethylpiperidine-1-oxyl (hydroxy TEMPO, 97%, Sigma Aldrich), was selected due to its high solubility in non-aqueous solvents and previous use in RFBs [4,38]. Permeability was measured using a 2-chamber glass cell where the donor chamber was filled with 3 mL of 0.1 M hydroxy

TEMPO and 0.5 M LiFSI in ACN and the receiving chamber was filled with 3 mL of 0.5 M LiFSI in ACN. The two chambers were separated by the sample membrane.

The concentration of hydroxy TEMPO in the receiver cell was measured at room temperature (22 °C) as a function of time using ultraviolet–visible (UV–Vis) spectroscopy and a linear calibration based on a unique absorbance peak measured at 455 nm. For hydroxy TEMPO, a linear calibration persisted for measurable concentrations from 0.8 to 20 mM hydroxy TEMPO in ACN (calibration can be found in Supporting Information, Fig. S5). As such, the chambers of the assembled cell were stirred for 3–12 h, depending on the permeability of the membrane. The timescale was chosen to ensure that the concentration of the receiving cell did not exceed 20 mM, which was the upper limit of the calibration curve.

To measure the concentration of hydroxy TEMPO in the receiver cell as a function of time ($C_r[t]$), the receiving chamber solution was transferred periodically to a UV–Vis cuvette. The hydroxy TEMPO concentration was determined using UV–Vis as described previously, and the solution was returned to the receiving chamber after the UV–Vis measurement. This process was repeated 3 times over the course of the experiment. Using the known initial donor concentration ($C_d[0]$), known chamber volume (V), measured membrane thickness (L), and known area (A) available for transport the permeability (P) can be related to $C_r[t]$ as:

$$Pt = \frac{VL}{A} * \ln\left(1 - 2 * \frac{C_r[t]}{C_d[0]}\right) \quad 4)$$

The permeability can then be calculated by plotting the right-hand side of equation (4) versus time and performing a linear regression.

2.6. Acetonitrile and electrolyte uptake

Membranes were cut into ¾ inch diameter circular disks and dried under vacuum at room temperature for approximately 16 h. The membranes were massed, then soaked in electrolyte solutions with concentrations ranging from 0 to 2 M LiFSI in ACN by 0.5 M increments. After 24 h (>24x the characteristic timescale for permeation, taken as L^2/P, in the samples based on the lowest hydroxy TEMPO permeability measured for the PEG-PPO membranes considered in this study), the membranes were wiped dry, to remove surface liquid, and quickly massed to determine the solvated mass of the membrane. This procedure was repeated after 48 h to ensure equilibrium uptake was attained.

The electrolyte uptake was determined as the percentage increase in mass of the membrane from the dry to the solvated state, normalized by the dry membrane mass. This electrolyte uptake included the mass of LiFSI salt and ACN present in the electrolyte-equilibrated membrane. The ACN uptake (i.e., the property reflecting the uptake of only ACN and not LiFSI) was calculated by subtracting the mass of the dry polymer $m_{m,dry}$ and the mass of the LiFSI salt sorbed within the membrane (m_{LiFSI}, see Section 2.7 for discussion on how this value was obtained) from the solvated membrane mass ($m_{m,solvated}$):

$$\text{ACN Uptake} = \frac{m_{m,solvated} - m_{LiFSI} - m_{m,dry}}{m_{m,dry}} \quad 5)$$

Similarly, the electrolyte mass fraction was calculated as:

$$\text{Mass Fraction of Electrolyte} = \frac{m_{m,solvated} - m_{m,dry}}{m_{m,solvated}} \quad 6)$$

2.7. LiFSI desorption

Membranes were dried under vacuum for approximately 16 h, massed, and then soaked in electrolyte solutions with concentrations ranging from 0 to 2 M LiFSI in ACN by 0.5 M increments. After 24 h of soaking, the membranes were wiped dry to remove residual electrolyte from the membrane surface. The thickness and width of a swollen membrane was measured with a micrometer and calipers, respectively, and the swollen membrane volume was determined geometrically. The membranes were then placed in aliquots of pure ACN to allow the sorbed LiFSI to desorb from the polymer over 24 h to ensure all the salt had desorbed from the membrane. The final conductivity of the desorption solution was measured using a Mettler Toledo Seven Compact conductivity probe at room temperature (22 °C). The concentration of LiFSI in this solution (C_{LiFSI}) was determined using a calibration curve for conductivity as a function of salt concentration (calibration can be found in Supporting Information, Fig. S6). Using this measured concentration, the volume of the ACN desorption solution (V_s), and the swollen membrane volume (V_M), the concentration of LiFSI in the solvated membrane (C_M) was determined as:

$$C_M = \frac{C_{LiFSI} V_s}{V_M} \quad 7)$$

3. Results and discussion

3.1. Polymer characterization

3.1.1. Structural analysis

The degree of functionalization of Br-PPO was verified using ^{1}H NMR spectroscopy (Table 1, a representative spectrum can be found in the Supporting Information, Fig. S2). The aliphatic and aromatic hydrogens on the PPO backbone were observed at 2.1 ppm and 6.5 ppm, respectively, with a shift to 4.3 ppm and 6.7 ppm resulting from the addition of bromine to one methyl group of the PPO repeat unit [3]. No peak was observed at 6.1 ppm indicating that bromine did not substitute at the aromatic position on the PPO repeat unit [3]. The degree of bromination

Table 1
Sample nomenclature, PEG oligomer properties and measures of PEG composition for the materials in this study.

Nomenclature (PEGa-PPOx)	PEG MW[a] [g/mol]	EG Repeat Units Per Chain[b]	Degree of Functionalization		PEG Content	
			Bromine[c]	PEG	By Mass	mEq (EG)/g (dry polymer)
PEG200-PPO9	200	4.5	0.09	0.08	12%	2.67
PEG200-PPO14			0.14	0.12	17%	3.91
PEG200-PPO18			0.18	0.155	21%	4.66
PEG400-PPO9	400	9.1	0.09	0.08	21%	4.78
PEG400-PPO14			0.14	0.125	29%	6.68
PEG400-PPO18			0.18	0.155	34%	7.73
PEG600-PPO9	600	13.6	0.09	0.08	29%	6.49
PEG600-PPO14			0.14	0.125	38%	8.73
PEG600-PPO18			0.18	0.155	44%	9.91

[a] Value of 'a' in the PEGa-PPOx nomenclature.
[b] Value of 'n' in Scheme 1.
[c] This value, multiplied by 100, is equal to 'x' in the PEGa-PPOx nomenclature.

Table 2
Composition data for PEG-PPO films based on DSC analysis. PEG content in the PPO-rich phase was determined by the glass transition temperatures of the films using the Fox equation.

Sample	Bulk Polymer PEG Content (mass %)	T_g (°C)	PEG Content based on the T_g (mass %)
Pure PPO	-	217	-
Pure PEG	-	−50	-
PEG200-PPO9	12	171	8
PEG200-PPO14	17	169	8
PEG200-PPO18	21	159	10
PEG400-PPO9	21	130	17
PEG400-PPO14	29	119	20
PEG400-PPO18	34	107	23
PEG600-PPO9	29	-	-
PEG600-PPO14	38	-	-
PEG600-PPO18	44	-	-

was calculated using the ratio of the integrated peaks at 4.3 and 2.1 ppm as [3]:

$$\text{Degree of Bromination} = \frac{2}{1 + \frac{2}{3} + \frac{peak\ (2.1\ ppm)}{peak\ (4.3\ ppm)}} \quad 8)$$

The PEG-PPO membranes were prepared using Br-PPO as an intermediate, with the intent to fully replace the bromine groups with PEG. The degree of bromination, found in Table 1, was used as a target for the degree of PEGylation, but the final degree of PEGylation was verified using ^{1}H NMR spectroscopy (a representative spectrum can be found in the Supporting Information, Fig. S2). The conversion of bromine to PEG resulted in shifts to the aliphatic hydrogens on the PEGylated methyl group of the PPO backbone from 4.3 to 4.4 ppm. Therefore, the disappearance of the peak at 4.3 ppm indicated conversion to PEG. Additional peaks were observed for the aliphatic hydrogens of the PEG chain and the free hydroxyl group at 3.6 and 1.7 ppm, respectively. To verify that complete functionalization had occurred, the degree of PEGylation of the final polymer, found in Table 1, was calculated in the same manner as the Br-PPO but replacing the integration of the peak at 4.3 with the integration of the peak at 4.4 in Equation (8).

The PEG content is reported in milli equivalents of ethylene glycol repeat units per gram of dry polymer, i.e., mEq (EG)/g (dry polymer) (Table 1). This relationship was used as it was analogous to ion exchange capacity (IEC), a term commonly used to describe the charge density in IEMs [17,24,49]. IEC describes the density of the charged side groups in the polymer on a gram of dry membrane basis. Generally, these charged groups are responsible for interactions with the counter-ions transported through the membrane [23]. In the PEG-PPO membranes, the ethylene glycol repeat units likely were responsible for ionic transport, so the PEG content was described accordingly. The PEG content, in units of mEq (EG)/g (dry polymer), was calculated using the molar mass of PEG, MW_{PEG}, the molar mass of PPO, MW_{PPO}, the molar mass of a single ethylene glycol repeat unit (MW_{EG}), and the degree of PEGylation of the polymer with the equation:

$$\frac{mEq\ (EG)}{g\ (dry\ polymer)} = \frac{DP}{(MW_{PPO} + DP * MW_{PEG})} * \frac{1000 * MW_{PEG}}{MW_{EG}} \quad 9)$$

3.1.2. Thermal analysis

A single, broad glass transition was observed for several of the PEG-PPO membranes indicating mixing between the PEG and PPO chains in the polymer matrix at all compositions (the DSC thermograms for all membranes studied in this work can be found in Supporting Information, Fig. S3). Increasing the PEG content of the membranes resulted in a gradual broadening of the glass transitions, and for the PEG600 membranes the glass transition was indiscernible. The broadening of the glass transitions was likely a result of heterogeneity in the polymer matrix afforded by the grafting of the PEG chains to the PPO backbone [50,51].

The glass transition temperatures of the PEG-PPO materials were suppressed relative to the glass transition temperature of the PPO homopolymer (Table 2). This observation suggests PEG mixing within a PPO-rich phase, perhaps facilitated by increased chain mobility afforded by the incorporation of PEG chains within the polymer [52–56]. The Fox equation [41] was used to estimate the PEG content in this PPO-rich phase based on the observed glass transition temperature for the polymer and the homopolymer glass transition temperatures (Table 2). A second glass transition temperature, which would indicate the presence of a PEG-rich phase, was not observed, and this situation may be the result of a relatively low PEG-rich phase composition within the materials. The experimentally measured glass transition temperatures were greater than those values obtained using the Fox Equation with the

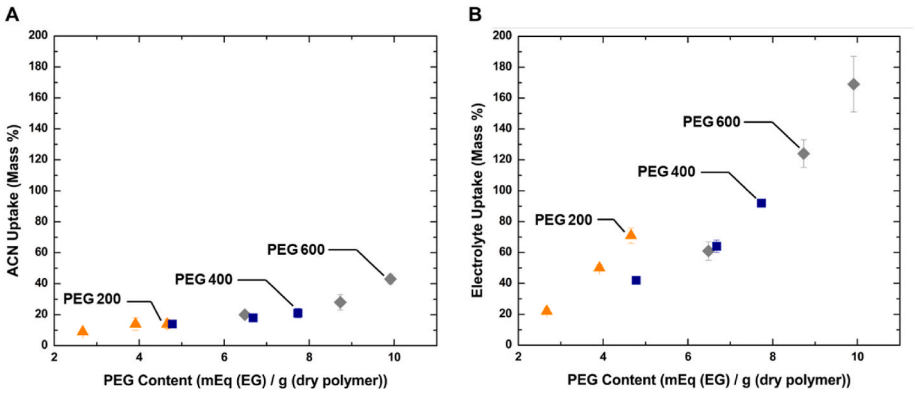

Fig. 2. (A) Solvent uptake of pure ACN into PEG-PPO membranes as a function of the PEG content (taken as the density of ethylene glycol side chains in units of mEq (EG)/g (dry polymer)) and (B) electrolyte (0.5 M LiFSI in ACN) uptake into PEG-PPO membranes as a function of the PEG content (taken as the density of ethylene glycol side chains in units of mEq (EG)/g (dry polymer)). The data are reported as the average of three measurements, and the uncertainty is quantified as one standard deviation from the mean.

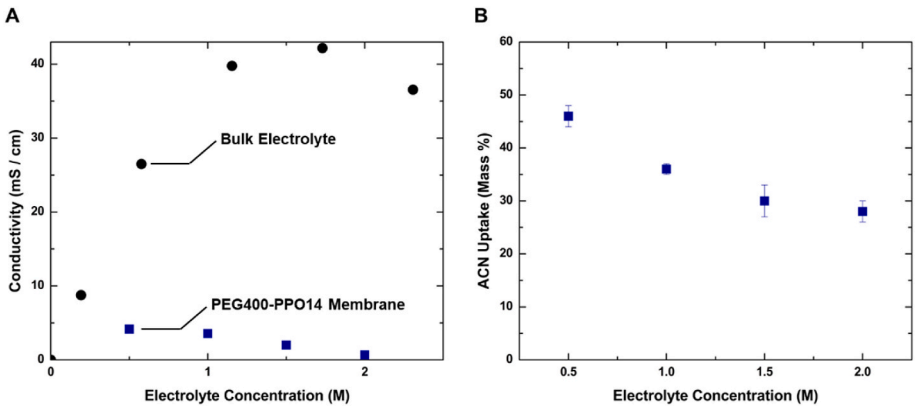

Fig. 3. (A) Conductivity of bulk electrolyte (LiFSI in ACN) and the PEG400-PPO14 membrane as a function of LiFSI concentration in the electrolyte and (B) ACN uptake of PEG400-PPO14 as a function of LiFSI concentration in the electrolyte. The data are reported as the average of three measurements, and the uncertainty is quantified as one standard deviation from the mean.

NMR-obtained PEG content of the synthesized PEG200 and PEG400 (Fig. S7), which further suggests phase behavior in this system that is not entirely captured by the DSC-based glass transition temperature measurements.

3.2. Acetonitrile uptake

For the membranes studied, ACN uptake increased as PEG content increased (Fig. 2A). This observation was likely a result of the polar ACN solvent (dielectric constant ~36) having a less favorable interaction with the PPO polymer backbone (with a dielectric constant of approximately 2.7) compared to the more polar PEG side chains (dielectric constants of 22.5, 17.4, and 14.3 for PEG200, 400, and 600 respectively at 25 °C) [57–59]. Similar behavior has been observed in IEMs in aqueous applications where favorable interactions between fixed charge on the polymer backbone and water promote water uptake in the membrane [60,61].

The role of PEG content in dictating solvent uptake can be further explored by comparing materials with the same PEG content but different PEG chain lengths and degrees of PEGylation. No significant difference in solvent uptake was observed for polymers with similar PEG repeat unit density but different side chain length (Fig. 2A). As such, the overall density of ethylene glycol repeat units, not side chain length or degree of PEGylation, appeared to drive solvent uptake behavior.

3.3. Electrolyte uptake

Exposing the membrane materials to 0.5 M LiFSI in ACN led to an increase in the electrolyte uptake (Fig. 2B) relative to the ACN uptake (without added electrolyte, Fig. 2A). Ethylene glycol has been shown to exhibit strong favorable interactions with LiFSI when used in SPEs [33,36,58,62]. Coupled with the solvation of LiFSI by ACN, the interactions between the ethylene glycol repeat units and LiFSI in solution results in a drastic increase in the overall electrolyte uptake. Similar behavior has been observed in a PPO-based anion exchange membrane where increased electrolyte uptake was attributed to the favorable interactions between the positive fixed charges of the polymer and the solvated electrolyte [63].

The electrolyte uptake of the PEG-PPO membranes may be sensitive to the PEG chain length of a given film. For example, PEG200-PPO18 had notably higher electrolyte uptake than that of PEG400-PPO9, even though both materials had approximately equivalent overall PEG content (Fig. 2B). At comparable density of ethylene glycol repeat units, PEG200-PPO18 contains shorter PEG chains spread throughout the polymer whereas PEG400-PPO9 contains half as many chains that are twice as long. This may create a difference in the way that the PEG

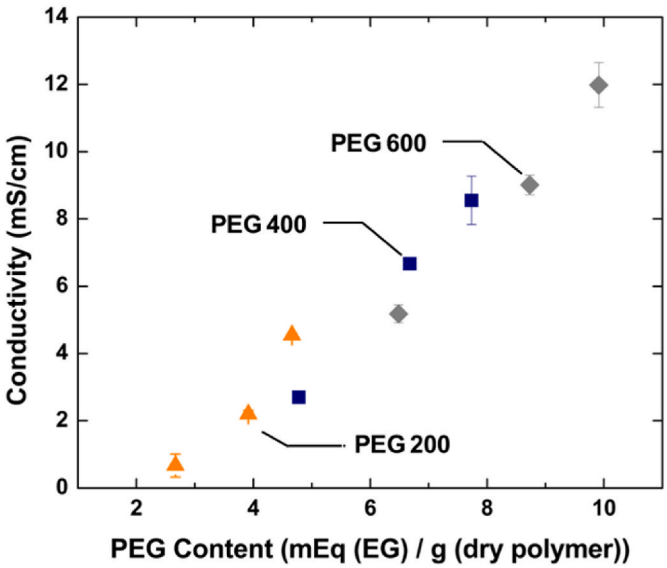

Fig. 4. Membrane conductivity in 0.5 M LiFSI in ACN as a function of PEG content (taken as the density of ethylene glycol side chains in units of mEq (EG)/g (dry polymer)). The data are reported as the average of three measurements, and the uncertainty is quantified as one standard deviation from the mean.

chains solvate with the electrolyte. In SPEs, it has been reported that approximately 4.5 ethylene glycol repeat units are necessary to solvate LiFSI [33]. In this case, it appears that the PEG200 films have a sufficient chain length, with ~4.5 repeat units per chain, to solvate LiFSI resulting in a spike in electrolyte uptake, as discussed. For the films with longer PEG chains, there are more ethylene glycol repeat units than are required for solvation of LiFSI, so it is possible that the ethylene glycol repeat units share the solvation of electrolyte within the membrane, which results in lower overall uptake at a given PEG content.

3.4. Ion transport

In solid polymer electrolytes, PEG chains have been successfully used to enhance conductivity because of favorable interactions with lithium-based electrolyte as well as a low glass transition temperature to promote chain mobility. In SPEs, ion conduction occurs via ion hopping between ethylene glycol repeat units and, therefore, increasing the PEG content of the polymer tends to increase conductivity [17,29,33,36,64]. In the PEG-PPO materials, the presence of electrolyte will significantly

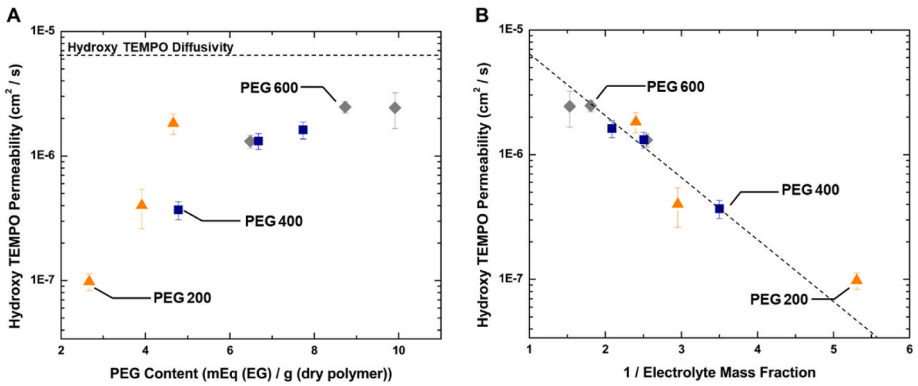

Fig. 5. (A) Hydroxy TEMPO permeability as a function of PEG content (taken as the density of ethylene glycol side chains in units of mEq (EG)/g (dry polymer)) and (B) semi log plot of hydroxy TEMPO permeability as a function of inverse mass fraction of electrolyte (0.5 M LiFSI in ACN) in the swollen polymer. Permeability was measured using 0.5 M LiFSI in ACN as the electrolyte. The data are reported as the average of three measurements, and the uncertainty is quantified as one standard deviation from the mean.

influence the transport of ions through the polymer. It is likely that ion conduction will occur through solvated regions of the membrane, perhaps in addition to ion hopping between ethylene glycol repeat units. Therefore, it is important to understand the influence of electrolyte, as well as polymer structure, on the conductivity of PEG-PPO membranes. Here, the influence of LiFSI concentration in the bulk electrolyte, PEG chain length, and degree of PEGylation on the conductivity of the membrane are discussed.

The conductivity of the PEG400-PPO14 film decreased as LiFSI concentration increased in the bulk electrolyte from 0.5 M to 2 M (Fig. 3A). This result contrasts the behavior in bulk LiFSI in ACN solution where the conductivity of LiFSI in ACN bulk electrolyte increases with increasing concentration until a peak value (above 40 mS/cm) is attained at a concentration of ~1.75 M (Fig. 3A). The swollen polymer behavior, where ionic conductivity decreased as LiFSI concentration increased, was consistent across all PEG-PPO membranes (the conductivity of all PEG-PPO membranes as a function of LiFSI concentration in the bulk electrolyte can be found in the Supporting Information, Fig. S8). The difference between the conductivity properties in bulk solution and in the membrane is likely caused by osmotic deswelling of the polymer with increasing LiFSI concentration in the bulk electrolyte. Such deswelling, where solvent content decreases as electrolyte concentration increases, is commonly observed in aqueous systems [45,60].

To further explore, ACN uptake was calculated from the LiFSI sorption and electrolyte uptake (described in Section 2.6). The ACN uptake of PEG400-PPO14 decreased as a function of LiFSI concentration in the bulk electrolyte, consistent with osmotic deswelling (Fig. 3B). The reduction in ACN uptake as electrolyte concentration increased (Fig. 3B) likely drove the reduction in conductivity with increasing electrolyte concentration (Fig. 3A) as ionic conductivity generally exhibits a positive correlation with solvent uptake [17].

For a fixed external electrolyte concentration, membrane conductivity tended to increase with increasing PEG content, as expected (Fig. 4). Furthermore, increasing the PEG chain length or the degree of PEGylation, while holding the other constant, resulted in an increase in the conductivity of the membrane (Fig. 4). In either case, the number of ethylene glycol repeat units in the membrane increased significantly with the modification to the polymer structure resulting in an increase in conductivity. The modification to the polymer structure also led to an increase in electrolyte uptake (Fig. 2B), which likely contributed to the increase in conductivity. It is unlikely that specific interactions resulting from changing the polymer structure significantly impacted the conductivity in this case. However, it does appear that the PEG chain length may influence the conductivity of a given membrane. For polymers with the same overall PEG content, the conductivity decreased as the PEG chain length of the membrane increased (~4.5 and ~6.5 mEq (EG)/g (dry polymer) in Fig. 4). As discussed previously, membranes functionalized with long PEG chains have a lower electrolyte uptake than those membranes with shorter PEG chains, possibly because the repeat units share the solvation of electrolyte within the membrane to a greater extent than is the case with the short chain systems. This decrease in solvation by the longer PEG chains may slow the conduction of ions through the polymer matrix relative to the short PEG chain case resulting in lower conductivity.

3.5. Redox active material permeability

Small molecule transport in polymer films has been widely ascribed to accessibility of small molecules to free volume elements within the polymer matrix [60]. Generally, as electrolyte uptake increases, the accessibility to free volume elements within the polymer increases, as does small molecule permeability. As previously described, increasing the PEG content of the PEG-PPO membranes resulted in an increase in electrolyte uptake due to favorable interactions between the PEG side chains and the electrolyte as well as solvation of both the PEG chains and LiFSI. Therefore, it was expected that the hydroxy TEMPO permeability would follow electrolyte uptake trends and increase with increasing PEG content.

In general, holding the PEG chain length constant, increasing the degree of PEGylation of the membrane resulted in an increase in the hydroxy TEMPO permeability, as expected (Fig. 5A). At a PEG content of ~4.5 mEq (EG)/g (dry polymer) the PEG400-PPO8 membrane had a lower permeability than the PEG200-PPO18 film (Fig. 5A). As discussed, the longer chain length of the PEG400 membranes resulted in a decrease in electrolyte uptake, so it is expected that the permeability would decrease in the PEG400 film. At PEG contents greater than 5 mEq (EG)/g (dry polymer), the hydroxy TEMPO permeability levels off as it approaches the diffusivity of hydroxy TEMPO in electrolyte (Fig. 5A). The diffusivity of hydroxy TEMPO in 0.5 M LiFSI in ACN was estimated to be 6.2×10^{-6} cm^2/s using the Wilke Chang model based on the reported viscosity of the electrolyte at 25 °C [42,65]. The leveling off behavior of the permeability likely resulted from the high electrolyte uptake of the polymer (>80%) where subsequent increases in electrolyte uptake resulted in relatively small changes to the hydroxy TEMPO permeability as free volume elements in the material were already readily accessible for transport.

To further examine the influence of electrolyte uptake on hydroxy TEMPO permeability, the electrolyte uptake in the materials was converted to electrolyte mass fraction, as described in Section 2.6, and these values were used to construct a semi-log plot of hydroxy TEMPO permeability versus the inverse electrolyte mass fraction (Fig. 5B) according to theory developed by Yasuda et al. [66] The observed

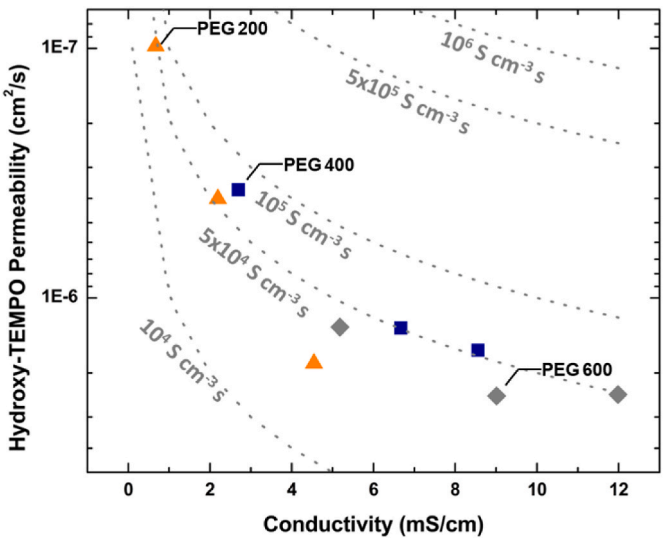

Fig. 6. Hydroxy TEMPO permeability and membrane ionic conductivity tradeoff plot. Note that the y-axis is inverted such that permeability decreases (favorable for flow battery applications) in the upward direction. The dotted lines are lines of constant selectivity. Selectivity increases as conductivity increases and permeability decreases (i.e., the upper right-hand corner of the plot corresponds to the highest values of selectivity.

exponential relationship between permeability and the inverse electrolyte mass fraction suggested that electrolyte uptake in these materials was a proxy for the free volume that facilitated hydroxy TEMPO permeation (Fig. 5B) [66–68]. Additionally, the correlation intersected the vertical axis, at an electrolyte mass fraction of unity (i.e., pure electrolyte), at a value that was consistent with the diffusivity of hydroxy TEMPO in 0.5 M LiFSI in ACN (Fig. 5B). This physically satisfying result has been observed in other non-aqueous and aqueous systems and further supports the position that the electrolyte uptake is critical for hydroxy TEMPO permeation in these materials [39,60,66]. Slight deviations away from the trendline may have resulted from second order affects influencing the redox molecule permeation such as second order interactions between the solvated polymer chains and the redox molecules in the electrolyte [38,60].

3.6. Selectivity for flow battery applications

In general, increasing PEG content led to an increase in both the permeability and conductivity of the membrane (Fig. 6). In redox flow battery applications, selectivity is defined as conductivity divided by permeability (meaning that selectivity for this application has units as illustrated on the dotted lines of Fig. 6). Often, as electrolyte uptake and ionic conductivity increase for a given polymer, a reduction in selectivity is observed. Such a situation was observed for the most highly functionalized PEG200 material and the two most highly functionalized PEG400 materials. The decrease in selectivity of the PEG400 material, however, was smaller compared to the situation for the PEG200 material, and the PEG600 material may actually realize increased selectivity at the highest degree of functionalization relative to the two lower degree of functionalization (and conductivity) materials. In particular, increasing the PEG content of the PEG400 and PEG600 materials led to increases in conductivity without dramatic reduction in selectivity.

4. Conclusions

PEG-PPO materials with varying PEG chain length and degree of PEGylation were successfully synthesized and fabricated into membranes. Increasing PEG content led to more favorable interactions between the membrane and ACN and, therefore, increased ACN uptake. Favorable interactions between ethylene glycol repeat units and LiFSI led to a dramatic increase in acetonitrile and electrolyte uptake when the materials were exposed to LiFSI. Increasing the LiFSI concentration in the bulk electrolyte, however, led to a decrease in ACN uptake and therefore a decrease in membrane conductivity due to osmotic deswelling. Hydroxy TEMPO permeability was consistent with free volume theory suggesting that the electrolyte uptake was the primary driver for transport in these films. Ultimately, increasing PEG content via PEG chain length and/or degree of PEGylation led to increased ionic conductivity, and the longer chain length PEG400 and PEG600 materials retained more of their selectivity as ionic conductivity increased.

CRediT authorship contribution statement

Charles R. Leroux: Writing – original draft, Visualization, Validation, Methodology, Investigation, Formal analysis, Data curation. **Patrick M. McCormack:** Visualization, Validation, Methodology, Conceptualization. **Shruti Elango:** Investigation, Data curation. **Geoffrey M. Geise:** Writing – review & editing, Supervision, Project administration, Funding acquisition, Conceptualization. **Gary M. Koenig:** Writing – review & editing, Supervision, Project administration, Funding acquisition, Conceptualization.

Declaration of competing interest

The authors declare the following financial interests/personal relationships which may be considered as potential competing interests: All authors report financial support was provided by the National Science Foundation. Geise is a member of the Polymer Editorial Advisory Board. The journal's editor-in-chief was one of Geise's Ph.D. thesis advisors. If there are other authors, they declare that they have no known competing financial interests or personal relationships that could have appeared to influence the work reported in this paper.

Data availability

Data will be made available on request.

Acknowledgements

This material is based upon work supported by the National Science Foundation under Grant No. 1940915. Any opinions, findings, and conclusions or recommendations expressed in this material are those of the author(s) and do not necessarily reflect the views of the National Science Foundation.

Appendix A. Supplementary data

Supplementary data to this article can be found online at https://doi.org/10.1016/j.polymer.2024.126986.

References

[1] A.Z. Weber, M.M. Mench, J.P. Meyers, P.N. Ross, J.T. Gostick, Q. Liu, Redox flow batteries: a review, J. Appl. Electrochem. 41 (10) (2011) 1137–1164, https://doi.org/10.1007/s10800-011-0348-2.
[2] J. Yuan, Z.-Z. Pan, Y. Jin, Q. Qiu, C. Zhang, Y. Zhao, Y. Li, Membranes in non-aqueous redox flow battery: a review, J. Power Sources 500 (2021) 229983, https://doi.org/10.1016/j.jpowsour.2021.229983.
[3] P.M. McCormack, H. Luo, G.M. Geise, G.M. Koenig, Conductivity, permeability, and stability properties of chemically tailored poly(phenylene oxide) membranes for Li+ conductive non-aqueous redox flow battery separators, J. Power Sources 460 (2020) 228107, https://doi.org/10.1016/j.jpowsour.2020.228107.
[4] J. Winsberg, T. Hagemann, T. Janoschka, M.D. Hager, U.S. Schubert, Redox-flow batteries: from metals to organic redox-active materials, Angew. Chem. Int. Ed. 56 (3) (2017) 686–711, https://doi.org/10.1002/anie.201604925.
[5] P. Alotto, M. Guarnieri, F. Moro, Redox flow batteries for the storage of renewable energy: a review, Renew. Sustain. Energy Rev. 29 (2014) 325–335, https://doi.org/10.1016/j.rser.2013.08.001.

[6] J. Chai, A. Lashgari, J. Jiang, "Jimmy." electroactive materials for next-generation redox flow batteries: from inorganic to organic, in: L. Qin, L.-S. Fan (Eds.), ACS Symposium Series, vol. 1364, American Chemical Society, Washington, DC, 2020, pp. 1–47, https://doi.org/10.1021/bk-2020-1364.ch001.

[7] G. Li, W. Chen, H. Zhang, Y. Gong, F. Shi, J. Wang, R. Zhang, G. Chen, Y. Jin, T. Wu, Z. Tang, Y. Cui, Membrane-free Zn/MnO_2 flow battery for large-scale energy storage, Adv. Energy Mater. 10 (9) (2020) 1902085, https://doi.org/10.1002/aenm.201902085.

[8] Z. Qi, G.M. Koenig, Review article: flow battery systems with solid electroactive materials, J. Vac. Sci. Technol. B Nanotechnol. Microelectron. Mater. Process. Meas. Phenom. 35 (4) (2017) 040801, https://doi.org/10.1116/1.4983210.

[9] Global Energy Review: CO2 Emissions in 2021. 2021, vol. 14.

[10] R. Darling, K. Gallagher, W. Xie, L. Su, F. Brushett, Transport property requirements for flow battery separators, J. Electrochem. Soc. 163 (1) (2016) A5029–A5040, https://doi.org/10.1149/2.0051601jes.

[11] R.M. Darling, K.G. Gallagher, J.A. Kowalski, S. Ha, F.R. Brushett, Pathways to low-cost electrochemical energy storage: a comparison of aqueous and nonaqueous flow batteries, Energy Environ. Sci. 7 (11) (2014) 3459–3477, https://doi.org/10.1039/C4EE02158D.

[12] N. Akhmetov, N. Ovsyannikov, N. Gvozdik, M. Pogosova, S. Ryazantsev, S. Lipovskikh, I. Krasnikova, K. Stevenson, Composite lithium-conductive LATP+PVdF membranes: development, optimization, and applicability for Li-TEMPO hybrid redox flow batteries, J. Membr. Sci. 643 (2022) 120002, https://doi.org/10.1016/j.memsci.2021.120002.

[13] C.M. Wong, C.S. Sevov, All-organic storage solids and redox shuttles for redox-targeting flow batteries, ACS Energy Lett. (2021) 1271–1279, https://doi.org/10.1021/acsenergylett.1c00143.

[14] V.P. Nemani, K.C. Smith, Analysis of crossover-induced capacity fade in redox flow batteries with non-selective separators, J. Electrochem. Soc. 165 (13) (2018) A3144–A3155, https://doi.org/10.1149/2.0701813jes.

[15] P. Leuaa, D. Priyadarshani, D. Choudhury, R. Maurya, M. Neergat, Resolving charge-transfer and mass-transfer processes of VO^{2+}/VO_2^+ redox species across the electrode/electrolyte interface using electrochemical impedance spectroscopy for vanadium redox flow battery, RSC Adv. 10 (51) (2020) 30887–30895, https://doi.org/10.1039/D0RA05224H.

[16] C. Jia, F. Pan, Y.G. Zhu, Q. Huang, L. Lu, Q. Wang, High–energy density nonaqueous all redox flow lithium battery enabled with a polymeric membrane, Sci. Adv. 1 (10) (2015) e1500886, https://doi.org/10.1126/sciadv.1500886.

[17] M.L. Lehmann, L. Tyler, E.C. Self, G. Yang, J. Nanda, T. Saito, Membrane design for non-aqueous redox flow batteries: current status and path forward, Chem 8 (6) (2022) 1611–1636, https://doi.org/10.1016/j.chempr.2022.04.005.

[18] L. Zhang, R. Feng, W. Wang, G. Yu, Emerging chemistries and molecular designs for flow batteries, Nat. Rev. Chem 6 (8) (2022) 524–543, https://doi.org/10.1038/s41570-022-00394-6.

[19] J.A. Kowalski, L. Su, J. milshtein, F.R. Brushett, Recent advances in molecular engineering for redox active organic molecules for nonaqeuous flow batteries, Curr. Opin. Chem. Eng. 13 (2016) 45–52, https://doi.org/10.1016/j.coche.2016.08.002.

[20] P. Leung, A.A. Shah, L. Sanz, C. Flox, J.R. Morante, Q. Xu, M.R. Mohamed, C. Ponce de León, F.C. Walsh, Recent developments in organic redox flow batteries: a critical review, J. Power Sources 360 (2017) 243–283, https://doi.org/10.1016/j.jpowsour.2017.05.057.

[21] F. Pan, Q. Wang, Redox species of redox flow batteries: a review, Molecules 20 (11) (2015) 20499–20517, https://doi.org/10.3390/molecules201119711.

[22] C.A. Machado, G.O. Brown, R. Yang, T.E. Hopkins, J.G. Pribyl, T.H. Epps, Redox flow battery membranes: improving battery performance by leveraging structure–property relationships, ACS Energy Lett. 6 (1) (2021) 158–176, https://doi.org/10.1021/acsenergylett.0c02205.

[23] L. Hu, L. Gao, M. Di, X. Jiang, X. Wu, X. Yan, X. Li, G. He, Ion/molecule-selective transport nanochannels of membranes for redox flow batteries, Energy Storage Mater. 34 (2021) 648–668, https://doi.org/10.1016/j.ensm.2020.10.008.

[24] T. Xu, Ion exchange membranes: state of their development and perspective, J. Membr. Sci. 263 (1–2) (2005) 1–29, https://doi.org/10.1016/j.memsci.2005.05.002.

[25] J. Ran, L. Wu, Y. He, Z. Yang, Y. Wang, C. Jiang, L. Ge, E. Bakangura, T. Xu, Ion exchange membranes: new developments and applications, J. Membr. Sci. 522 (2017) 267–291, https://doi.org/10.1016/j.memsci.2016.09.033.

[26] A.J. Butzelaar, P. Röring, T.P. Mach, M. Hoffmann, F. Jeschull, M. Wilhelm, M. Winter, G. Brunklaus, P. Théato, Styrene-based poly(ethylene oxide) side-chain block copolymers as solid polymer electrolytes for high-voltage lithium-metal batteries, ACS Appl. Mater. Interfaces 13 (33) (2021) 39257–39270, https://doi.org/10.1021/acsami.1c08841.

[27] C. Ding, H. Zhang, X. Li, H. Zhang, C. Yao, D. Shi, Morphology and electrochemical properties of perfluorosulfonic acid ionomers for vanadium flow battery applications: effect of side-chain length, ChemSusChem 6 (7) (2013) 1262–1269, https://doi.org/10.1002/cssc.201300014.

[28] A. Eisenberg, Clustering of ions in organic polymers. A theoretical approach, Macromolecules 3 (2) (1970) 147–154, https://doi.org/10.1021/ma60014a006.

[29] M. Rezayani, F. Sharif, H. Makki, Role of side-chain lengths on hydronium mobility in sulfonated poly(ether Sulfone) proton-conducting model membranes, J. Phys. Chem. C 127 (18) (2023) 8462–8472, https://doi.org/10.1021/acs.jpcc.3c01026.

[30] Y. Jiang, X. Yan, Z. Ma, P. Mei, W. Xiao, Q. You, Y. Zhang, Development of the PEO based solid polymer electrolytes for all-solid state lithium ion batteries, Polymers 10 (11) (2018) 1237, https://doi.org/10.3390/polym10111237.

[31] J. Ping, H. Pan, P. Hou, M.-Y. Zhang, X. Wang, C. Wang, J. Chen, D. Wu, Z. Shen, X.-H. Fan, Solid polymer electrolytes with Excellent high-temperature properties based on Brush block copolymers having rigid side chains, ACS Appl. Mater. Interfaces 9 (7) (2017) 6130–6137, https://doi.org/10.1021/acsami.6b15893.

[32] B. Wang, H. Lou, H. Xu, J. Zhao, Q. Wang, Q. Shi, Y. Deng, High voltage, solvent-free solid polymer electrolyte based on a star-comb PDLLA–PEG copolymer for lithium ion batteries, RSC Adv. 8 (12) (2018) 6373–6380, https://doi.org/10.1039/C7RA13664A.

[33] Y. Zhao, L. Wang, Y. Zhou, Z. Liang, N. Tavajohi, B. Li, T. Li, Solid polymer electrolytes with high conductivity and transference number of Li ions for Li-based rechargeable batteries, Adv. Sci. 8 (7) (2021) 2003675, https://doi.org/10.1002/advs.202003675.

[34] C. Cao, Y. Li, S. Chen, C. Peng, Z. Li, L. Tang, Y. Feng, W. Feng, Electrolyte-solvent-modified alternating copolymer as a single-ion solid polymer electrolyte for high-performance lithium metal batteries, ACS Appl. Mater. Interfaces 11 (39) (2019) 35683–35692, https://doi.org/10.1021/acsami.9b10595.

[35] A. Panday, S. Mullin, E.D. Gomez, N. Wanakule, V.L. Chen, A. Hexemer, J. Pople, N.P. Balsara, Effect of molecular weight and salt concentration on conductivity of block copolymer electrolytes, Macromolecules 42 (13) (2009) 4632–4637, https://doi.org/10.1021/ma900451e.

[36] Z. Xue, D. He, X. Xie, Poly(Ethylene oxide)-based electrolytes for lithium-ion batteries, J. Mater. Chem. A 3 (38) (2015) 19218–19253, https://doi.org/10.1039/C5TA03471J.

[37] X. Peng, H. Ba, D. Chen, F. Wang, Two-component epoxy network-LiClO4 polymer electrolyte, Electrochim. Acta 37 (9) (1992) 1569–1572, https://doi.org/10.1016/0013-4686(92)80113-Z.

[38] P.M. McCormack, G.M. Koenig, G.M. Geise, Thermodynamic interactions as a descriptor of cross-over in nonaqueous redox flow battery membranes, ACS Appl. Mater. Interfaces 13 (41) (2021) 49331–49339, https://doi.org/10.1021/acsami.1c14845.

[39] P.M. McCormack, G.M. Koenig, G.M. Geise, Transport property modulation via solvent-specific behavior in crosslinked nonaqueous membranes, ACS Appl. Polym. Mater. 5 (4) (2023) 2449–2461, https://doi.org/10.1021/acsapm.2c02121.

[40] A. Diamanti, Z. Ganase, E. Grant, A. Armstrong, P.M. Piccione, A.M. Rea, J. Richardson, A. Galindo, C.S. Adjiman, Mechanism, kinetics and selectivity of a Williamson ether synthesis: elucidation under different reaction conditions, React. Chem. Eng. 6 (7) (2021) 1195–1211, https://doi.org/10.1039/D0RE00437E.

[41] P. Hiemenz, T. Lodge, Polymer Chemistry, CRC Press, 2007.

[42] S.-D. Han, O. Borodin, D.M. Seo, Z.-B. Zhou, W.A. Henderson, Electrolyte solvation and ionic association: V. Acetonitrile-lithium bis(Fluorosulfonyl)Imide (LiFSI) mixtures, J. Electrochem. Soc. 161 (14) (2014) A2042–A2053, https://doi.org/10.1149/2.0101414jes.

[43] J.D. Milshtein, R.M. Darling, J. Drake, M.L. Perry, F.R. Brushett, The critical role of supporting electrolyte selection on flow battery cost, J. Electrochem. Soc. (2017).

[44] L. Cao, A. Kronander, A. Tang, D.-W. Wang, M. Skyllas-Kazacos, Membrane Permeability Rates of Vanadium Ions and Their Effects on Temperature Variation in Vanadium Redox Batteries, 2016.

[45] J. Peng, T.A. Zawodzinski, Describing ion exchange membrane-electrolyte interactions for high electrolyte concentrations used in electrochemical reactors, J. Membr. Sci. 593 (2020) 117340, https://doi.org/10.1016/j.memsci.2019.117340.

[46] H. Cesiulis, N. Tsyntsaru, A. Ramanavicius, G. Ragoisha, The study of thin films by electrochemical impedance spectroscopy, in: I. Tiginyanu, P. Topala, V. Ursaki (Eds.), Nanostructures and Thin Films for Multifunctional Applications, NanoScience and Technology, Springer International Publishing, Cham, 2016, pp. 3–42, https://doi.org/10.1007/978-3-319-30198-3_1.

[47] V. Vivier, M.E. Orazem, Impedance analysis of electrochemical systems, Chem. Rev. 122 (12) (2022) 11131–11168, https://doi.org/10.1021/acs.chemrev.1c00876.

[48] D.A. Harrington, P. van den Driessche, Mechanism and equivalent circuits in electrochemical impedance spectroscopy, Electrochim. Acta 56 (23) (2011) 8005–8013, https://doi.org/10.1016/j.electacta.2011.01.067.

[49] P. Xiong, L. Zhang, Y. Chen, S. Peng, G. Yu, A chemistry and microstructure perspective on ion-conducting membranes for redox flow batteries, Angew. Chem. Int. Ed. 60 (47) (2021) 24770–24798, https://doi.org/10.1002/anie.202105619.

[50] V.A. Kusuma, G. Gunawan, Z.P. Smith, B.D. Freeman, Gas permeability of cross-linked poly(ethylene-oxide) based on poly(ethylene glycol) dimethacrylate and a miscible siloxane Co-monomer, Polymer 51 (24) (2010) 5734–5743, https://doi.org/10.1016/j.polymer.2010.09.069.

[51] V.A. Kusuma, B.D. Freeman, S.L. Smith, A.L. Heilman, D.S. Kalika, Influence of TRIS-based Co-monomer on structure and gas transport properties of cross-linked poly(ethylene oxide), J. Membr. Sci. 359 (1–2) (2010) 25–36, https://doi.org/10.1016/j.memsci.2010.01.049.

[52] K. Chang, A. Korovich, T. Xue, W.A. Morris, L.A. Madsen, G.M. Geise, Influence of rubbery versus glassy backbone dynamics on multiscale transport in polymer membranes, Macromolecules 51 (22) (2018) 9222–9233, https://doi.org/10.1021/acs.macromol.8b01830.

[53] N.S. Vrandečić, M. Erceg, M. Jakić, I. Klarić, Kinetic analysis of thermal degradation of poly(ethylene glycol) and poly(ethylene Oxide)s of different molecular weight, Thermochim. Acta 498 (1–2) (2010) 71–80, https://doi.org/10.1016/j.tca.2009.10.005.

[54] T.A. Speckhard, K.K.S. Hwang, S.B. Lin, S.Y. Tsay, M. Koshiba, Y.S. Ding, S. L. Cooper, Properties of UV curable polurethane acrylates: effect of reactive diluent, J. Appl. Polym. Sci. (1984).

[55] S. Pal, R. Mondal, S. Guha, U. Chatterjee, S.K. Jewrajka, Crosslinked terpolymer anion exchange membranes for selective ion separation and acid recovery, J. Membr. Sci. 612 (2020) 118459, https://doi.org/10.1016/j.memsci.2020.118459.

[56] K. Jin, J.M. Torkelson, Tg and Tg breadth of poly(2,6-dimethyl-1,4-phenylene oxide)/polystyrene miscible polymer blends characterized by differential scanning calorimetry, ellipsometry, and fluorescence spectroscopy, Polymer 65 (2015) 233–242, https://doi.org/10.1016/j.polymer.2015.04.016.
[57] L.G. Gagliardi, C.B. Castells, C. Ràfols, M. Rosés, E. Bosch, Static dielectric constants of acetonitrile/water mixtures at different temperatures and Debye−Hückel A and $a_0 B$ parameters for activity coefficients, J. Chem. Eng. Data 52 (3) (2007) 1103–1107, https://doi.org/10.1021/je700055p.
[58] W.-Q. Ding, F. Lv, N. Xu, M.-T. Wu, J. Liu, X.-P. Gao, Polyethylene oxide-based solid-state composite polymer electrolytes for rechargeable lithium batteries, ACS Appl. Energy Mater. 4 (5) (2021) 4581–4601, https://doi.org/10.1021/acsaem.1c00216.
[59] R. Sengwa, K. Kaur, R. Chaudhary, Dielectric properties of low molecular weight poly(ethylene Glycol)s, Polym. Int. 49 (6) (2000) 599–608, https://doi.org/10.1002/1097-0126(200006)49:6<599::AID-PI425>3.0.CO, 2-K.
[60] G.M. Geise, D.R. Paul, B.D. Freeman, Fundamental water and salt transport properties of polymeric materials, Prog. Polym. Sci. 39 (1) (2014) 1–42, https://doi.org/10.1016/j.progpolymsci.2013.07.001.
[61] G.M. Geise, B.D. Freeman, D.R. Paul, Characterization of a sulfonated pentablock copolymer for desalination applications, Polymer 51 (24) (2010) 5815–5822, https://doi.org/10.1016/j.polymer.2010.09.072.
[62] C.S. Kim, S.M. Oh, Importance of donor number in determining solvating ability of polymers and transport properties in gel-type polymer electrolytes, Electrochim. Acta 45 (13) (2000) 2101–2109, https://doi.org/10.1016/S0013-4686(99)00426-0.
[63] Y. Li, J. Sniekers, J.C. Malaquias, C. Van Goethem, K. Binnemans, J. Fransaer, I.F. J. Vankelecom, Crosslinked anion exchange membranes prepared from poly (phenylene oxide) (PPO) for non-aqueous redox flow batteries, J. Power Sources 378 (2018) 338–344, https://doi.org/10.1016/j.jpowsour.2017.12.049.
[64] I.A. Stenina, Ph. Sistat, A.I. Rebrov, G. Pourcelly, A.B. Yaroslavtsev, Ion mobility in nafion-117 membranes, Desalination 170 (1) (2004) 49–57, https://doi.org/10.1016/j.desal.2004.02.092.
[65] C.R. Wilke, P. Chang, Correlation of diffusion coefficients in dilute solutions, AIChE J. 1 (2) (1955) 264–270, https://doi.org/10.1002/aic.690010222.
[66] H. Yasuda, C. Lamaze, L. Ikenberry, Permeability of solutes through hydrated polymer membranes, Makromol. Chem. 118 (2858) (1968) 19–35.
[67] G.M. Geise, H.-S. Lee, D.J. Miller, B.D. Freeman, J.E. McGrath, D.R. Paul, Water purification by membranes: the role of polymer science, J. Polym. Sci., Part B: Polym. Phys. 48 (15) (2010) 1685–1718, https://doi.org/10.1002/polb.22037.
[68] W. Xie, H. Ju, G.M. Geise, B.D. Freeman, J.I. Mardel, A.J. Hill, J.E. McGrath, Effect of free volume on water and salt transport properties in directly copolymerized disulfonated poly(Arylene ether Sulfone) random Copolymers, Macromolecules 44 (11) (2011) 4428–4438, https://doi.org/10.1021/ma102745s.